Published in final edited form as:
Nat Nanotechnol. 2013 December ; 8(12): 952–958. doi:10.1038/nnano.2013.219.

Highly efficient gate-tunable photocurrent generation in vertical heterostructures of layered materials

Woo Jong Yu[1,2,3], **Yuan Liu**[4], **Hailong Zhou**[1], **Anxiang Yin**[1], **Zheng Li**[1], **Yu Huang**[4,5], and **Xiangfeng Duan**[1,5]

Xiangfeng Duan: xduan@chem.ucla.edu

[1]Department of Chemistry and Biochemistry, University of California, Los Angeles, California 90095, USA

[2]Department of Electronic and Electrical Engineering, Sungkyunkwan University, Suwon 440-746, Republic of Korea

[3]Center for Integrated Nanostructure Physics, Institute for Basic Science (IBS), Sungkyunkwan University, Suwon 440-746, Republic of Korea

[4]Department of Materials Science and Engineering, University of California, Los Angeles, California 90095, USA

[5]California Nanosystems Institute, University of California, Los Angeles, California 90095, USA

Abstract

Layered materials of graphene and MoS_2, for example, have recently emerged as an exciting material system for future electronics and optoelectronics. Vertical integration of layered materials can enable the design of novel electronic and photonic devices. Here, we report highly efficient photocurrent generation from vertical heterostructures of layered materials. We show that vertically stacked graphene–MoS_2–graphene and graphene–MoS_2–metal junctions can be created with a broad junction area for efficient photon harvesting. The weak electrostatic screening effect of graphene allows the integration of single or dual gates under and/or above the vertical heterostructure to tune the band slope and photocurrent generation. We demonstrate that the amplitude and polarity of the photocurrent in the gated vertical heterostructures can be readily modulated by the electric field of an external gate to achieve a maximum external quantum efficiency of 55% and internal quantum efficiency up to 85%. Our study establishes a method to control photocarrier generation, separation and transport processes using an external electric field.

Correspondence to: Xiangfeng Duan, xduan@chem.ucla.edu.

Author contributions

X.D. conceived the research. X.D. and W.J.Y. designed the experiment. W.J.Y. performed most of the experiments, including device fabrication, characterization and data analysis. Y.L. helped W.J.Y. with photocurrent measurements. H.Z. synthesized the grapheme samples. A.Y. performed the reflectance measurements. Z.L. performed the simulations. Y.H. and X.D. supervised the research. X.D. and W.J.Y. co-wrote the paper. All authors discussed the results and commented on the manuscript.

Additional information

Supplementary information is available in the online version of the paper. Reprints and permissions information is available online at www.nature.com/reprints.

Competing financial interests

The authors declare no competing financial interests.

Layered materials such as graphene have attracted considerable interest for possible applications in diverse electronic and optoelectronic devices[1–6], including transistors[7–13], photodetectors[14–18], ultrafast lasers[19], polarizers[20], touch panels[21] and optical modulators[22]. With its broad spectral absorption[23], high carrier mobility[24] and short carrier lifetime[25], graphene exhibits exciting potential for wideband, high-speed photodetection[14–18]. However, the intrinsically weak absorption characteristics and small built-in potential in these graphene-based photodetectors have severely limited their external quantum efficiency (EQE) to the range of ~0.1–1% (refs 16,17). Also, to date, the design of graphene-based photodetectors has usually largely relied on a lateral metal–graphene– metal junction with a rather small photoresponsive active area near the graphene–metal contact, which is not ideal for efficient photon harvesting[14–18]. Similar lateral metal–MoS_2–metal devices based on few-layer MoS_2 have also been reported with a relatively small photoresponsivity of ~0.1 AW^{-1} (ref. 26). Here, we report highly efficient photocurrent generation from vertically stacked graphene–MoS_2–graphene and graphene–MoS_2–metal junctions.

Vertical graphene–MoS_2–graphene devices

Figure 1 presents a schematic illustration of a graphene– MoS_2–graphene vertical heterostructure device on a Si/SiO_2 substrate. The device fabrication procedures are described in the Methods (Supplementary Fig. 1). A confocal laser was used to generate electron–hole pairs in the MoS_2 layer, which can be separated by the asymmetric potential in the top graphene (Gr_T)–MoS_2 and bottom graphene (Gr_B)–MoS_2 junctions to produce a measurable photocurrent (Fig. 1a,b). The current–voltage (I_{DS}–V_{DS}) data obtained in the dark (blue line, Fig. 1c) and under 514 nm laser irradiation (red line, Fig. 1c) show a clear photoresponse in the vertical heterostructure, with an open-circuit voltage of ~0.3 V and short-circuit current of ~2 μA. In general, the photoresponse exhibits a rapid temporal response beyond our experimental time resolution of 50 μs (Supplementary Fig. 2), demonstrating that the photoresponse originates from photocarrier generation rather than any other extrinsic effects.

Single-gated graphene–MoS_2–graphene devices

Figure 2a,b presents an optical image and scanning electron microscope (SEM) image of a typical vertical heterostructure device. The 8 μm strip of Gr_B (red in Fig. 2b) is located under the MoS_2 flake (blue in Fig. 2b), and the Gr_T layer (yellow in Fig. 2b) is located directly above the MoS_2 flake to overlap with Gr_B to ensure vertical charge transport. The thickness of the MoS_2 flake was determined by atomic force microscopy (AFM) to be ~50 nm. The underlying silicon substrate functions as a back gate to modulate charge transport across the graphene–MoS_2–graphene vertical stack. The I_{DS}–V_{DS} measurements of the device under dark conditions at various back-gate biases (V_{BG}) indicate that the device exhibits n-type characteristics (Supplementary Fig. 3), which is consistent with the intrinsically n-type nature of the MoS_2 layer[11]. Additionally, all the I_{DS}–V_{DS} curves in the dark, at variable gate voltages, pass through the origin (dark curve in Fig. 2c and Supplementary Fig. 3), indicating that there is no gate leakage that could interfere with photocurrent measurement. For the measurement of photocurrent, the device was tested

under focused laser illumination at variable V_{BG}. A series of I_{DS}–V_{DS} plots show that the short-circuit current I_{sc} and open-circuit voltage V_{oc} can be readily modulated by V_{BG} (Fig. 2c), with both I_{sc} and V_{oc} increasing with decreasing V_{BG} (Fig. 2c, inset).

To further probe the photoresponse characteristics of the device, we conducted scanning photocurrent measurements under a confocal optical microscope. A series of scanning photocurrent (I_{ph}) images of the device were taken under short-circuit conditions at different V_{BG} between −60 and 60 V (Fig. 2d). The Gr_B and Gr_T electrodes are highlighted in the photocurrent images by dashed and solid lines, respectively. Unlike graphene-based lateral photodetectors, which have a rather small photosensing active area near the graphene– metal contact, the vertical heterostructure device clearly shows broad-area photocurrent generation throughout the entire area of the vertical graphene–MoS_2–graphene stack. The image taken at V_{BG} = +60 V shows a strong photocurrent in the area where Gr_T and Gr_B overlap, demonstrating that the photoresponsive area covers the entire vertical stack. With the gate voltage stepping in a negative direction, the overall photocurrent increases and the photoresponsive area also appears to expand beyond the area of overlapping Gr_B and Gr_T. In particular, the photocurrent image for V_{BG} = −60 V shows that the photoresponse can be observed from the entire MoS_2 flake. This observation demonstrates that the photocarriers generated outside the vertical stack can also contribute to the overall photocurrent and suggests that the minority carrier diffusion length in our devices is at least on the micrometre scale.

Overall, the ability to modulate the photocurrent with an external back-gate voltage indicates that it is possible to manipulate the photocarrier generation, separation and transport processes in such vertically stacked devices. These experimental observations can be explained by using the band diagrams of the vertical stack under various back-gate voltages (Fig. 2e–h, Supplementary Fig. 4). Before applying a back gate, the initial built-in potential is determined by the Schottky barrier height difference between the Gr_T–MoS_2 and Gr_B–MoS_2 contacts. Because the channel length (~50 nm) is much shorter than the total depletion length (~140–170 nm) near both graphene–MoS_2 contacts (Supplementary Fig. 5), the top and bottom Schottky barriers merge together to form a monotonic band slope across the entire stack. This band slope determines the separation and transport of the excited electrons and holes. In our device, the Schottky barrier height in the Gr_B–MoS_2 contact is higher than that of the Gr_T–MoS_2 contact, probably due to a p-type doping effect to the graphene by the substrate oxide[27]. As a result, the band in the MoS_2 layer slopes downward towards the top contact with a built-in field that drives excited electrons to move towards the Gr_T (Fig. 2e).

Importantly, with the finite density of states in graphene and weak electrostatic screening effect[9–12], the Gr_B–MoS_2 Schottky barrier height can be effectively modulated by an external field applied through the back-gate electrode V_{BG}. With negative V_{BG}, the workfunction of the Gr_B increases and so does the Gr_B–MoS_2 Schottky barrier height, which increases the band slope in MoS_2 to further promote the electron–hole separation and enhance the photocurrent (Fig. 2f). On the other hand, a positive V_{BG} decreases the Gr_B–MoS_2 Schottky barrier and reduces the band slope in MoS_2 to suppress the electron–hole separation and reduce the overall photocurrent (Fig. 2g). In principle, when the positive V_{BG} is large enough, the Schottky barrier height of the Gr_B–MoS_2 junction can be decreased to

be lower than that of the Gr_T–MoS_2 junction, thus inverting the band slope and switching the photocurrent into the negative regime (Fig. 2h). However, this switching effect was not observed in this device before dielectric breakdown under increasing gate voltage, but is readily observable in dual-gated devices (Fig. 3).

Based on the photocurrent response and input laser power, we can determine the EQE of the device. The EQE (η) is defined as the number of carriers produced per photon, or

$$\eta = \frac{I_{\mathrm{ph}}}{q\phi} = \frac{I_{\mathrm{ph}}}{q}\left(\frac{hv}{p_{\mathrm{opt}}}\right)$$

where I_{ph} is the photocurrent, φ is the photon flux (= P_{opt}/hv), h is Planck's constant, v is the frequency of light, q is the electron charge and P_{opt} is the optical power[28]. Our study shows that the EQE can be increased from ~6% at V_{BG} = 60 V to ~15% at V_{BG} = −60 V under excitation by 80 μW laser power (Fig. 2i). Furthermore, it is found that the EQE increases with decreasing excitation laser power and saturates at ~27% when the excitation laser power is <5 μW (Fig. 2i, inset). The EQE observed in these vertical graphene–MoS_2–graphene heterostructure devices is much higher than that of lateral metal–graphene–metal photodetectors (EQE ≈ 0.1%)[14]. This higher EQE can be largely attributed to more efficient photon absorption in the broad-area vertical heterostructure with multilayer MoS_2, as well as more efficient charge separation resulting from a much larger and tunable band offset. EQE values obtained at various excitation powers and wavelengths from another device (with 16-nm-thick MoS_2) show a similar trend, with the signature of saturation at a power of 10 μW or below (Fig. 2j). The decreasing EQE with increasing excitation power could be attributed partly to absorption saturation in MoS_2 (Supplementary Fig. 6a) and partly to the screening of a built-in electric field by the excited electrons in the conduction band of MoS_2. The wavelength-dependent EQE plot shows two peak EQE values at ~480 nm and ~600 nm (black line in Fig. 2k), which can be largely attributed to the absorbance peaks in MoS_2 (red line in Fig. 2k and Supplementary Fig. 6b) and is consistent with previous studies[29, 30]. Taking the optical absorption of the MoS_2 layer into account, the maximum internal quantum efficiency (IQE) of this device is estimated to be ~85% (blue line, Fig. 2k).

Dual-gated graphene–MoS_2–graphene devices

To further probe the ability to tune the photocurrent with an external field, we created an additional top-gate electrode on top of the graphene–MoS_2–graphene stack, using 60 nm HfO_2 as the insulating dielectric layer and another layer of graphene as the transparent top-gate electrode (Gr_G)[31] (Fig. 3a). The transfer characteristics of a typical dual-gated vertical heterostructure device (Fig. 3b) are shown in Fig. 3c. Each curve was obtained by sweeping the back-gate bias V_{BG} from −60 to +60 V at a fixed drain–source bias V_{DS} of 100 mV while stepping the top-gate bias V_{TG} from −6 to +4 V in steps of 1 V. The transfer characteristics exhibit n-type behaviour (dominated by n-type MoS_2) versus V_{BG}, with two kinks corresponding to the Dirac points of Gr_T (red arrow, Fig. 3c) and Gr_B (blue arrow, Fig. 3c). The Dirac points of the Gr_T (solid line) and Gr_B (dashed line) can also be seen in the two-dimensional image of the transconductance (dI/dV_{BG}) in Fig. 3d. Overall, the Dirac point of

the Gr_B is only slightly shifted from V_{BG} = −32 V to −27 V by varying V_{TG} due to the weak coupling between the Gr_B and the top gate, while the Dirac point of the Gr_T can be greatly shifted from −60 V to +40 V by varying V_{TG} due to the much stronger gate coupling between the Gr_T and the top gate. When V_{TG} is small (~0 V), the Dirac points of both Gr_T and Gr_B almost match at $V_{BG} \approx -30$ V. With positive V_{TG}, the Gr_T Dirac point shifts to be lower than that of the Gr_B, and with a negative V_{TG} the Gr_T Dirac point shifts to be higher than that of the Gr_B.

Modulation of the Dirac points of the Gr_T and Gr_B can directly impact the amplitude and direction of the band slope in the MoS_2 layer, as shown in the band diagrams under different top- or back-gate voltages (Fig. 3e–h). Simulated band diagrams are shown in Supplementary Fig. 4. With the back-gate bias set near the Gr_B Dirac point (V_{BG} = −30 V), a negative V_{TG} increases the workfunction of Gr_T, resulting in a higher Schottky barrier in the Gr_T–MoS_2 contact than in the Gr_B–MoS_2 contact, with a downward band slope in MoS_2 towards Gr_B, which drives the excited electrons towards Gr_B to produce a negative photocurrent (Fig. 3e). When V_{TG} is small (around 0 V), the Gr_T and Gr_B have similar Dirac points around V_{BG} = −30 V; there is little band slope or driving force for the separation and transport of excited electrons and holes (Fig. 3f), resulting in negligible photocurrent. When V_{TG} is increased to a positive value, the band slope in MoS_2 switches its direction to slope downwards towards Gr_T to drive the excited electrons moving towards the Gr_T and produce a positive photocurrent (Fig. 3g). A sequence of scanning photocurrent images of the device taken under short-circuit conditions at V_{BG} = −30 V and different values of V_{TG} between −6 and 6 V clearly shows that the photocurrent can be readily switched from negative values ($V_{TG}<0$) to nearly zero (V_{TG} = 0), followed by positive values ($V_{TG}>0$) (Fig. 3i). With a negative V_{TG} that increases the workfunction of Gr_T, applying $V_{BG}> -30$ V reduces the workfunction of Gr_B, which can further increase the band slope in MoS_2 and enhance the negative photocurrent (Fig. 3h,j). Overall, within the dual-gated graphene– MoS_2–graphene heterostructure, the amplitude of the photocurrent can be greatly modulated and the polarity of the photocurrent can be completely switched by the external gate field. For example, the photocurrent obtained at V_{BG} = 60 V and V_{TG} = −6 V is more than 500 times larger than that at V_{BG} = −30 V and V_{TG} = 0 V.

In an alternative and probably more simplified picture, the generation and polarity of the photocurrent within the dual-gated vertical devices can be easily understood without considering the details within the graphene–MoS_2–graphene stack. In general, the polarity and amplitude of the overall photocurrent is largely determined by the field direction and field strength across the top and bottom gates, with the photogenerated electrons (holes) always moving towards the positively (negatively) biased gate electrode. Unlike conventional photodiodes in which the photocarrier separation and transport are dictated by the internal built-in potential and are barely changeable with any external factors, our study clearly demonstrates that, with the partial electrostatic transparency of graphene, the photocarrier separation, transport and photocurrent generation processes in the vertical graphene–MoS_2–graphene devices can be substantially manipulated by an external field.

Single-gated graphene–MoS_2–metal device

The above studies were based on a nearly symmetric graphene– MoS_2–graphene stack. We also explored an asymmetrical vertical heterostructure of graphene–MoS_2–metal (Ti) for photocurrent generation. With a graphene–MoS_2 Schottky contact and a nearly ohmic MoS_2–Ti contact[11], the asymmetric device could allow for further enhancement of the photocurrent. With the opaque metal electrode on the top of the stack, the device was fabricated on the glass substrate with a 100 nm transparent indium tin oxide (ITO) thin film as the back-gate electrode and a 30 nm Al_2O_3 thin film as the gate dielectrics, to allow for excitation laser illumination from the back side of the substrate to reach the graphene–MoS_2– metal stack (Fig. 4a,b, Supplementary Fig. 7).

In the vertical heterostructure of the graphene–MoS_2–metal (Ti) stack (Fig. 4c), the top MoS_2–Ti forms a nearly ohmic contact, while the Gr_B–MoS_2 contact forms a Schottky junction (Supplementary Fig. 4). Accordingly, the energy band in the MoS_2 slopes downwards towards the top contact, and the amplitude of the slope can be modulated by the potential applied through the back-gate electrode. A negative V_{BG} increases the workfunction of Gr_B and the Schottky barrier height of the Gr_B–MoS_2 contact (Fig. 4d), which induces additional band bending and increases the band slope in MoS_2 to promote electron–hole separation and photocurrent generation. A positive V_{BG} decreases the Schottky barrier height of the Gr_B–MoS_2 junction and reduces the band slope in MoS_2 to suppress the photocurrent (Fig. 4e). A sequence of scanning photocurrent images of the device taken under short-circuit conditions at variable V_{BG} are shown in Fig. 4f. The measurement at $V_{BG} = -1$ V displays a strong photocurrent in the overlapping area of the Gr_B and Ti electrodes. The photocurrent gradually decreases with increasing gate voltage in the positive direction. A series of *I*–*V* plots obtained under laser illumination show that both the open-circuit voltage and short-circuit current increase with negative V_{BG} and decrease with positive V_{BG} (Fig. 4g). EQE measurements obtained at various excitation powers and wavelengths show that the EQE gradually increases with decreasing power and saturates at a power of 10 μW or less (Fig. 4h), similar to the results for graphene–MoS_2–graphene devices (Fig. 2j). Importantly, a maximum photocurrent EQE of 55% (corresponding to a photoresponsivity of ~0.22 AW^{-1}) is achieved at an excitation wavelength of 488 nm (Fig. 4i).

Discussion

In summary, we have shown that vertical heterostructures of graphene– MoS_2–graphene and graphene–MoS_2–metal stacks can be created to obtain highly efficient photocurrent generation and photodetection. We further demonstrate that both a top- and bottom-gate can be integrated within the vertical heterostructure to create dual-gated graphene–MoS_2–graphene devices, which allows us to use an external electrical field to modulate the amplitude or even completely reverse the polarity of the photocurrent in the vertical junctions.

Although gate modulation of photocurrent has been reported in lateral metal–graphene–metal junctions[14–17] and top-gate induced lateral p–n junctions in graphene devices[32], it is

important to note that the modulating field in such lateral devices is perpendicular to the charge separation/transport direction, and the external field modulates the band-bending and built-in potential in the lateral junctions to indirectly tune the charge separation and transport processes. In contrast, the external field direction in the vertical device is parallel to the current direction and can directly modulate the charge separation and transport. This capability is enabled by several unique characteristics of such vertical heterostructures, including (1) the optical transparency of graphene, (2) the partial 'electrostatic transparency' of graphene due to its finite density of states and weak electrostatic screening effect, and (3) the ultrathin nature of the layered semiconductor (MoS_2) sandwiched between. Within the unique architecture of the vertical heterostructure, the top and bottom Schottky barriers are merged together in the ultrathin semiconducting layer to form a monotonic band slope. This band slope dictates the separation and transport of the excited electrons and holes and is highly tunable by an external field across the dual-gate electrodes. This is in stark contrast to conventional photodiodes or the recently reported graphene–silicon junctions[33, 34], in which the photocurrent is dictated by the internal built-in potential. It should also be noted that the use of the external gate field to modulate the photoresponsivity in the vertical heterostructure is entirely different from directly biased photodiodes (metal–semiconductor or p–n diodes). For example, directly biasing the graphene–MoS_2–graphene stack or any conventional photodiodes would greatly increase the dark current and power consumption, whereas the gated devices in our studies operate at zero bias voltage, and the capacitively coupled external gate field does not generate any additional dark current. These unique features of the vertical heterostructures will open up exciting opportunities for the design of future photodetection and photovoltaic devices.

During the peer-review process of this manuscript, we became aware of another study on a similar topic[35]. Our study was developed independently.

Methods

Fabrication of the vertical heterostructure devices

To fabricate the vertical graphene–MoS_2–graphene devices, graphene was grown using a chemical vapour deposition process[36–40] and transferred onto a Si/SiO_2 (300 nm SiO_2) substrate, then patterned into 8 μm × 30 μm strips to obtain a bottom electrode using photolithography and oxygen plasma etching processes. The MoS_2 flakes were then exfoliated onto the graphene strips through a micromechanical cleavage approach[38]. The top graphene electrode was transferred and patterned onto the stacked MoS_2 flake and bottom graphene. The directly overlapping graphene area was patterned and etched away to avoid shorting between the top and bottom graphene. The metal electrodes (for probe contact or wire bonding purposes) were patterned on the bottom and top graphene electrodes by electron-beam lithography and electronbeam deposition of Ti/Au (50/50 nm) thin film. For the dual-gated heterostructure devices, a 60-nm-thick HfO_2 dielectric layer was deposited by electron-beam evaporation. The gate graphene electrode was transferred onto HfO_2 and patterned using electron-beam lithography. For the graphene–MoS_2–metal heterostructure devices, ITO glass with a 30 nm Al_2O_3 dielectric layer was used as the supporting substrate

to allow illumination from the back side. The Al_2O_3 dielectric layer was deposited by an atomic layer deposition method.

Microscopic and optoelectrical characterizations

SEM imaging was performed on a JEOL 6700F unit operated at 5 kV. Electrical transport measurements were conducted with a probe station equipped with a computer-controlled analog-todigital converter at room temperature. The scanning photocurrent measurements were conducted with the same electrical measurement system under a SP2 MP Film confocal microscope coupled with an Ar/ArKr laser (wavelengths of 458, 476, 488, 496 and 514 nm) and a HeNe laser (543, 596 and 633 nm).

Supplementary Material

Refer to Web version on PubMed Central for supplementary material.

Acknowledgments

The authors acknowledge technical support from the Nanoelectronics Research Facility at UCLA. X.D. acknowledges partial support from a National Science Foundation CAREER award (DMR-0956171) and an Office of Naval Research Young Investigator Award (N00014-12-1-0745). W.J.Y. acknowledges partial support from a National Research Foundation of Korea grant funded by the Korean Government (Ministry of Education, Science and Technology; NRF-2011-351-c00034) and the Institute for Basic Science in Korea. Y.H. acknowledges support from the National Institutes of Health Director's New Innovator Award Program (1DP2OD007279). Z.L. is a visiting student from the Department of Physics, Peking University, sponsored by the UCLA cross-disciplinary scholars in science and technology (CSST) programme.

References

1. Novoselov KS, et al. A roadmap for grapheme. Nature. 2012; 490:192–200. [PubMed: 23060189]
2. Weiss NO, et al. Graphene: an emerging electronic material. Adv. Mater. 2012; 24:5782–5825. [PubMed: 22930422]
3. Schwierz F. Graphene transistors. Nature Nanotech. 2010; 5:487–496.
4. Bonaccorso F, Sun Z, Hasan T, Ferrari AC. Graphene photonics and optoelectronics. Nature Photon. 2010; 4:611–622.
5. Avouris P. Graphene: electronic and photonic properties and devices. Nano Lett. 2010; 10:4285–4294.
6. Bao Q, Loh KP. Graphene photonics, plasmonics, and broadband optoelectronic devices. ACS Nano. 2012; 6:3677–3694. [PubMed: 22512399]
7. Lin YM, et al. Wafer-scale graphene integrated circuit. Science. 2011; 10:1294–1297. [PubMed: 21659599]
8. Liao L, et al. High-speed graphene transistors with a self-aligned nanowire gate. Nature. 2010; 467:305–308. [PubMed: 20811365]
9. Britnell L, et al. Field-effect tunneling transistor based on vertical graphene heterostructure. Science. 2012; 335:947–950. [PubMed: 22300848]
10. Yang H, et al. Graphene barristor, a triode device with a gate-controlled schottky barrier. Science. 2012; 336:1140–1143. [PubMed: 22604723]
11. Yu WJ, et al. Vertically stacked multi-heterostructures of layered materials for logic transistors and complementary inverters. Nature Mater. 2013; 12:246–252. [PubMed: 23241535]
12. Georgiou T, et al. Vertical field-effect transistor based on grapheme–WS_2 heterostructures for flexible and transparent electronics. Nature Nanotech. 2013; 8:100–103.
13. Haigh SJ, et al. Cross-sectional imaging of individual layers and buried interfaces of graphene-based heterostructures and superlattices. Nature Mater. 2012; 11:764–767. [PubMed: 22842512]

14. Xia F, Mueller T, Lin YM, Valdes-Garcia A, Avouris P. Ultrafast graphene photodetector. Nature Nanotech. 2009; 4:839–843.
15. Mueller T, Xia F, Avouris P. Graphene photodetectors for high-speed optical communications. Nature Photon. 2010; 4:297–301.
16. Liu Y, et al. Plasmon resonance enhanced multicolour photodetection by graphene. Nature Commun. 2011; 2:579. [PubMed: 22146398]
17. Echtermeyer T, et al. Strong plasmonic enhancement of photovoltage in graphene. Nature Commun. 2011; 2:458. [PubMed: 21878912]
18. Sun D, et al. Ultrafast hot-carrier-dominated photocurrent in graphene. Nature Nanotech. 2012; 7:114–118.
19. Sun Z, et al. Graphene mode-locked ultrafast laser. ACS Nano. 2010; 4:803–810. [PubMed: 20099874]
20. Bao Q, et al. Broadband graphene polarizer. Nature Photon. 2011; 5:411–415.
21. Bae S, et al. Roll-to-roll production of 30-inch graphene films for transparent electrodes. Nature Nanotech. 2010; 5:574–478.
22. Liu M, et al. A graphene-based broadband optical modulator. Nature. 2011; 474:64–67. [PubMed: 21552277]
23. Nair RR, et al. Fine structure constant defines visual transparency of graphene. Science. 2008; 320:1308–1308. [PubMed: 18388259]
24. Chen JH, Jang C, Xiao S, Ishigami M, Fuhrer MS. Intrinsic and extrinsic performance limits of graphene devices on SiO_2. Nature Nanotech. 2008; 3:206–209.
25. Hwang E, Hu BYK, Sarma SD. Inelastic carrier lifetime in graphene. Phys. Rev. B. 2007; 76:115434.
26. Fontana M, et al. Electron–hole transport and photovoltaic effect in gated MoS_2 Schottky junction. Sci. Rep. 2013; 3:1634. [PubMed: 23567328]
27. Ryu S, et al. Atmospheric oxygen binding and hole doping in deformed on a SiO_2 substrate. Nano Lett. 2010; 10:4944–4951. [PubMed: 21069971]
28. Sze, SM.; Ng, KK. Physics of Semiconductor Devices. Wiley; 2007.
29. Eda G, et al. Photoluminescence from chemically exfoliated MoS_2. Nano Lett. 2011; 11:5111–5116. [PubMed: 22035145]
30. Mak KF, Lee C, Hone J, Shan J, Heinz TF. Atomically thin MoS_2: a new direct-gap semiconductor. Phys. Rev. Lett. 2010; 105:136805. [PubMed: 21230799]
31. Nair RR, et al. Fine structure constant defines visual transparency of graphene. Science. 2008; 320:1308. [PubMed: 18388259]
32. Lemme MC, et al. Gate-activated photoresponse in a graphene p–n junction. Nano Lett. 2011; 11:4134–4137. [PubMed: 21879753]
33. Li X, et al. Graphene-on-silicon Schottky junction solar cells. Adv. Mater. 2010; 22:2743–2748. [PubMed: 20379996]
34. Miao X, et al. High efficiency graphene solar cell by chemical doping. Nano. Lett. 2012; 12:2745–2750. [PubMed: 22554195]
35. Britnell L, et al. Strong light–matter interactions in heterostructures of atomically thin films. Science. 2013; 340:1311–1314. [PubMed: 23641062]
36. Reina A, et al. Large area, few-layer graphene films on arbitrary substrates by chemical vapor deposition. Nano Lett. 2009; 9:30–35. [PubMed: 19046078]
37. Li X, et al. Large-area synthesis of high quality and uniform graphene films on copper foils. Science. 2009; 324:1312–1314. [PubMed: 19423775]
38. Liu L, et al. A systematic study of atmospheric pressure chemical vapor deposition growth of large-area monolayer grapheme. J. Mater. Chem. 2012; 22:1498–1503. [PubMed: 25414547]
39. Zhou H, et al. Chemical vapour deposition growth of large single crystals of monolayer and bilayer graphene. Nature Commun. 2013; 4:2096. [PubMed: 23803650]
40. Radisavljevic B, Radenovic A, Brivio1 J, Giacometti V, Kis A. Single-layer MoS_2 transistors. Nature Nanotech. 2011; 6:147–150.

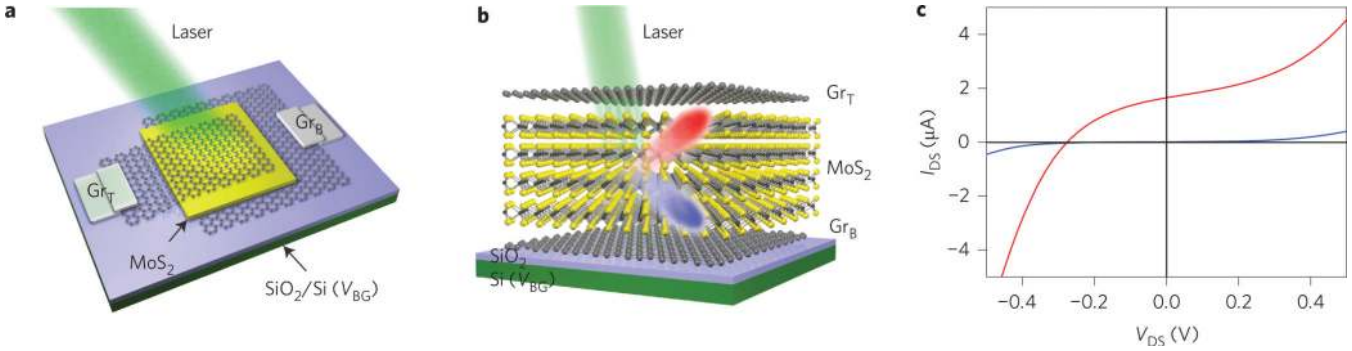

Figure 1. Photocurrent generation in vertical heterostructures of graphene–MoS_2–graphene

a, Schematic illustration of the three-dimensional device layout. **b**, Schematic illustration of the side view of the device, with the semiconducting multilayer MoS_2 sandwiched between the Gr_T and Gr_B electrodes. Red and blue colours indicate electrons and holes, respectively. The silicon substrate can be used as a back-gate electrode with 300 nm SiO_2 as the dielectric layer. **c**, Experimental current–voltage characteristic of the vertical device in the dark (blue) and under illumination (red) by a focused laser beam (wavelength, 514 nm; power, 80 μW; spot size, 1 μm).

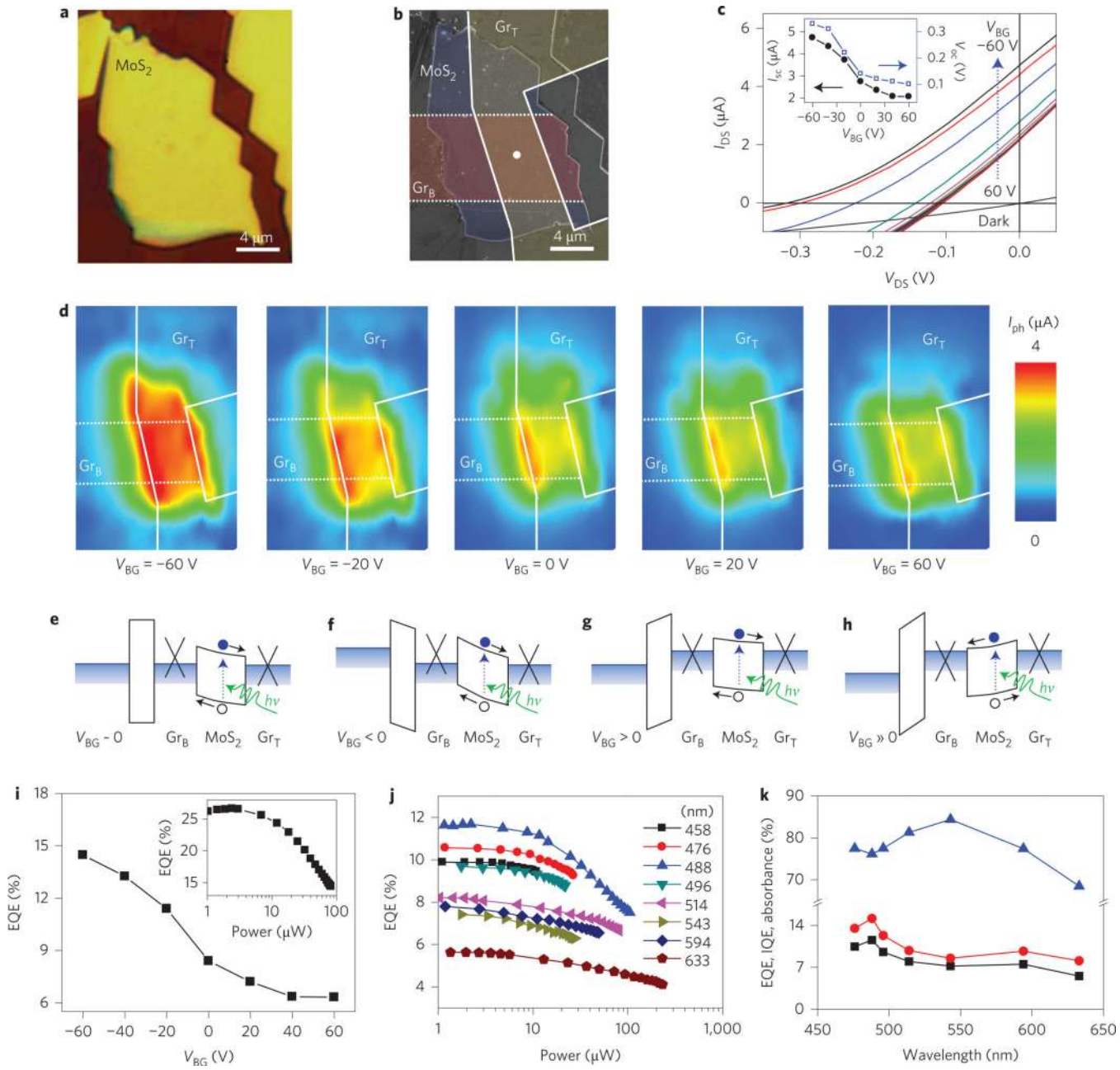

Figure 2. Field-effect modulated photocurrent generation in single-gated graphene–MoS_2–graphene heterostructures

a, Optical image of the vertical heterostructure with a multilayer MoS_2 flake (~50 nm thick) sandwiched between the Gr_T and Gr_B electrodes. **b**, SEM image of the same device with the Gr_T (yellow), Gr_B (red) and intermediate MoS_2 layer (blue) labelled with different false colours. **c**, I–V characteristics of the device under laser illumination (on white dot in **b**) at V_{BG} varying from −60 V to +60 V in steps of 20 V. Inset: variation of I_{sc} and V_{oc} with V_{BG}. **d**, Scanning photocurrent images taken at gate biases between −60 V and +60 V under a 514 nm laser (excitation power, 80 μW; spot size, 1 μm). Dashed and solid lines indicate the edges of the Gr_B and Gr_T electrodes, respectively. **e–h**, Schematic band diagrams of the

vertical heterostructure with zero (**e**), negative (**f**), positive (**g**) and large positive (**h**) bias on the silicon back gate. Blue dots, black circles and green arrows indicate electrons, holes and photons, respectively. **i**, EQE of the vertical heterostructure device as a function of back-gate voltage under 80 μW, 514 nm laser excitation. Inset: EQE of the device as a function of excitation laser power at $V_{BG} = -60$ V. **j**, Excitation laser power-dependent EQE of another graphene-MoS_2 (16 nm)-graphene device under various excitation wavelengths at $V_{BG} = -60$ V. **k**, Wavelength-dependent EQE (black line with squares), absorbance (red line with circles) and IQE (blue line with triangles) of the device at $V_{BG} = -60$ V under a focused laser power of 5 μW.

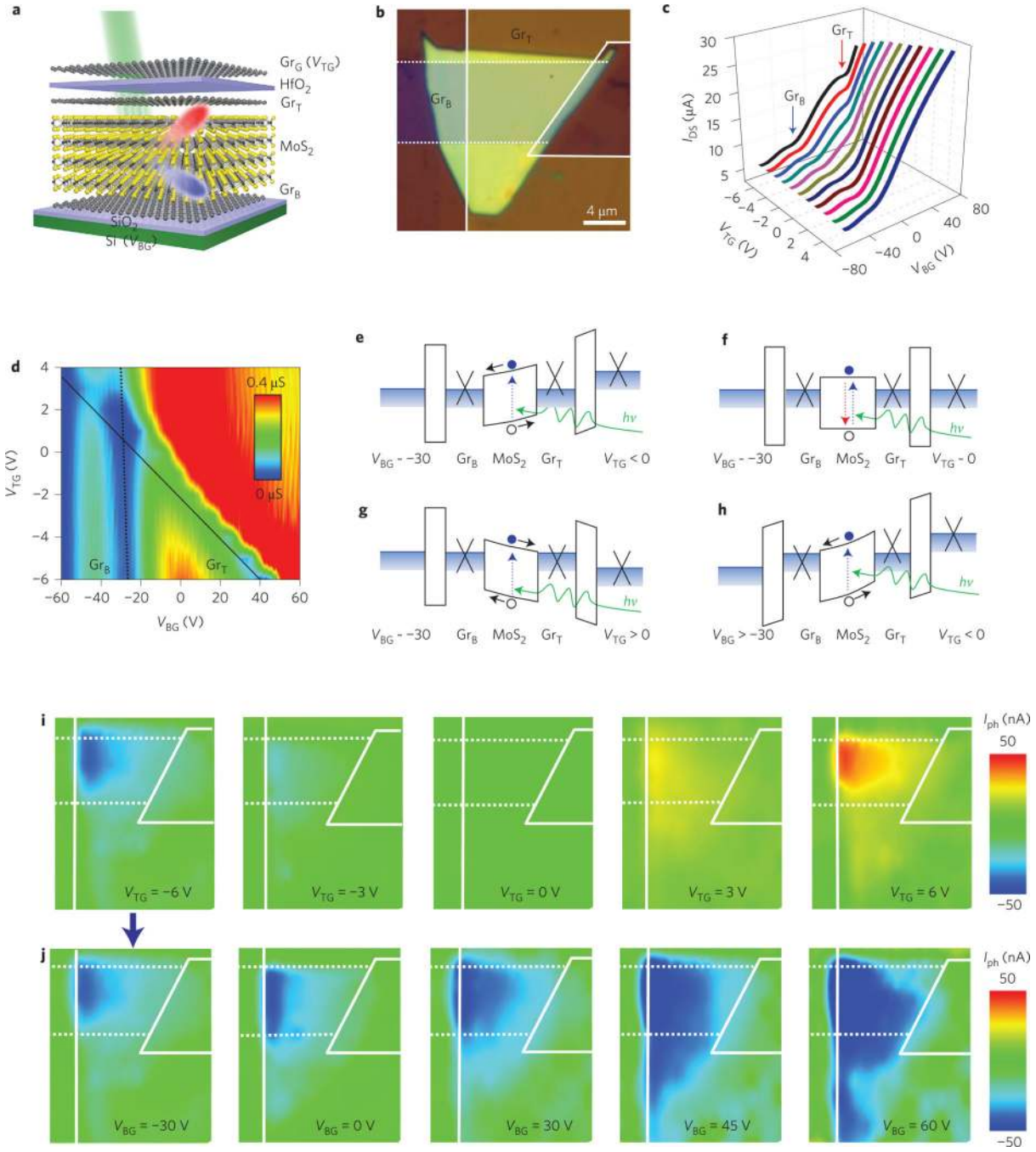

Figure 3. Field-effect switchable photocurrent generation in dual-gated graphene–MoS_2–graphene heterostructures

a, Schematic illustration of the side view of the device, with a multilayer MoS_2 flake sandwiched between the Gr_T and Gr_B electrodes, the silicon substrate as a back-gate electrode with a 300 nm SiO_2 dielectric layer, and another graphene layer as the top-gate electrode (Gr_G) with a 60 nm HfO_2 gate dielectric layer. **b**, Optical image of a dualgated device. **c**, Transfer characteristics of a dual-gated vertical heterostructure device as a function of V_{BG} (−60 V to +60 V) at various V_{TG} (−6 V to +4 V) at V_{DS} = 100 mV. Blue

and red arrows indicate the Dirac points of the Gr_B and Gr_T electrodes, respectively. **d**, Two-dimensional colour plot of the transconductance (dI_{DS}/dV_{BG}) of the dual-gated vertical heterostructure device. The Dirac points of the Gr_T and Gr_B electrodes are shown by solid and dashed lines, respectively. **e–g**, Schematic band diagrams of the dual-gated vertical heterostructure device with negative, zero and positive top-gate bias at a back-gate bias near the bottom graphene Dirac point (−30 V). The red dashed arrow in **f** indicates the recombination of electrons and holes. **h**, Schematic band diagram of the device with negative top-gate bias and more positive back-gate bias than the Gr_B Dirac point −30 V to further enhance the band slope and overall photocurrent. **i**, Scanning photocurrent images taken at V_{BG} = −30 V and variable V_{TG} (−6 V to +6 V) (under 80 μW, 514 nm laser excitation, with a spot size of 1 μm). Dashed and solid lines indicate the edges of the Gr_B and Gr_T electrodes, respectively. **j**, Scanning photocurrent images taken at fixed V_{TG} = −6 V and variable V_{BG} (−30 to +60 V).

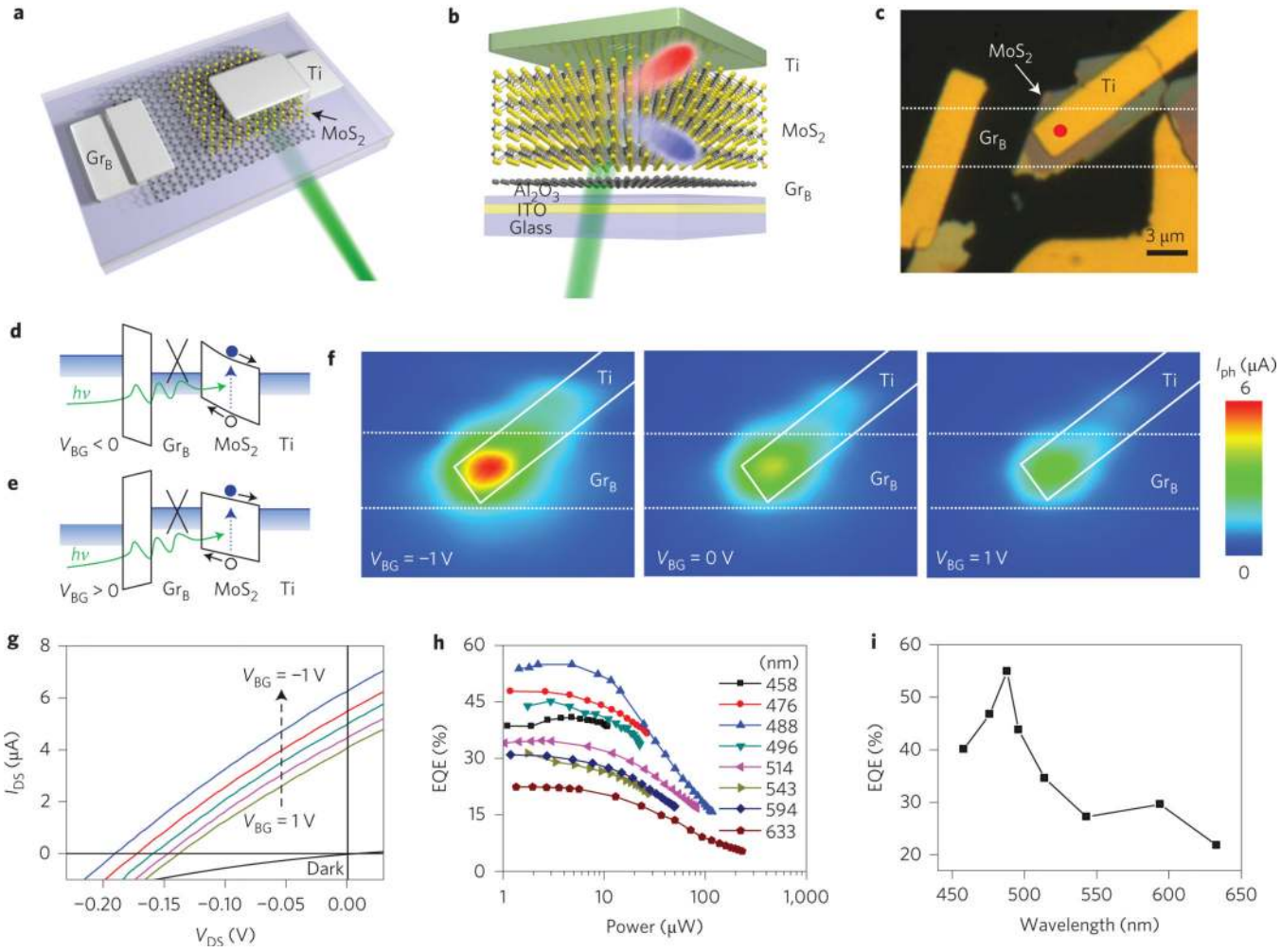

Figure 4. Field-effect modulated photocurrent generation in a single-gated graphene–MoS_2–metal heterostructure

a, Schematic three-dimensional illustration of the device layout. **b**, Schematic illustration of the side view of the device, with a multilayer MoS_2 flake sandwiched between a Gr_B electrode and a top metal electrode (Ti). The device was fabricated on transparent ITO on a glass substrate (as the back gate) with 30-nm-thick Al_2O_3 as the gate dielectric to allow illumination to transmit through the back side of the substrate to reach the graphene–MoS_2 contact. **c**, Optical image of a graphene–MoS_2–metal heterostructure device. **d,e**, Schematic band diagrams of the graphene–MoS_2–metal heterostructure at negative and positive back-gate voltages, respectively. **f**, Scanning photocurrent images taken at V_{BG} = −1, 0 and +1 V (80μW, 514 nm excitation, with a spot size of 1 μm). Dashed and solid lines indicate the edges of the Gr_B and top metal electrodes, respectively. **g**, I–V characteristics of the device under laser illumination (on red dot in **c**) with V_{BG} varying from −1 V to 1 V in steps of 0.5 V. The I–V curve obtained in the dark at V_{BG} = −1 V passes through the origin, indicating that gate leakage is negligible. **h**, Excitation laser power-dependent EQE under various excitation wavelengths at V_{BG} = −1 V. **i**, Wavelength-dependent EQE at a laser power of 5 μW.